

¹ **Multiscale Computational Framework to Investigate Integrin Mechanosensing and
2 Cell Adhesion**

³ Andre R. Montes,¹ Gabriela Gutierrez,¹ Adrian Buganza Tepole,^{2, a)} and Mohammad
⁴ R.K. Mofrad^{1, b)}

⁵ *^{1) Department of Mechanical Engineering, University of California, Berkeley,}
^{6 CA}*

⁷ *^{2) School of Mechanical Engineering, Purdue University, West Lafayette,}
^{8 IN}*

⁹ (*Electronic mail: abuganza@purdue.edu, mofrad@berkeley.edu)

¹⁰ (Dated: 26 August 2023)

^{a)}Tepole Mechanics & Mechanobiology Lab: engineering.purdue.edu/tepolelab/

^{b)}Molecular Cell Biomechanics Lab: biomechanics.berkeley.edu

11 ABSTRACT

12 Integrin mechanosensing plays an instrumental role in cell behavior, phenotype, and fate by
13 transmitting mechanical signals that trigger downstream molecular and cellular changes. For in-
14 stance, force transfer along key amino acid residues can mediate cell adhesion. Disrupting key
15 binding sites within $\alpha_5\beta_1$ integrin's binding partner, fibronectin (FN) diminishes adhesive strength.
16 While past studies have shown the importance of these residues in cell adhesion, the relationship
17 between the dynamics of these residues and how integrin distributes force across the cell sur-
18 face remains less explored. Here, we present a multiscale mechanical model to investigate the
19 mechanical coupling between integrin nanoscale dynamics and whole-cell adhesion mechanics.
20 Our framework leverages molecular dynamics simulations to investigate residues within $\alpha_5\beta_1$ -FN
21 during stretching and the finite element method to visualize the whole-cell adhesion mechanics.
22 The forces per integrin across the cell surface of the whole-cell model were consistent with past
23 atomic force microscopy and Förster resonance energy transfer measurements from literature. The
24 molecular dynamics simulations also confirmed past studies that implicate two key sites within FN
25 that maintain cell adhesion: the synergy site and RGD motif. Our study contributed to our under-
26 standing of molecular mechanisms by which these sites collaborate to mediate whole-cell integrin
27 adhesion dynamics. Specifically, we showed how FN unfolding, residue binding/unbinding, and
28 molecular structure contribute to $\alpha_5\beta_1$ -FN's nonlinear force-extension behavior during stretching.
29 Our computational framework could be used to explain how the dynamics of key residues influ-
30 ence cell differentiation or how uniquely designed protein structures could dynamically limit the
31 spread of metastatic cells.

32 I. INTRODUCTION

33 Cell-matrix junctions, governed in part by macromolecular structures known as focal adhesions
34 (FAs), can alter cell phenotype, behavior, and fate via applied mechanical signals that trigger
35 downstream molecular and cellular changes^{1–9}. At the heart of FA formation is a transmembrane
36 heterodimer known as integrin containing α - and β - subunits. Normally, nascent FAs initiate
37 with integrin activation, where cytoplasmic proteins bind to the integrin tails and the integrin head
38 extends to an active state with a higher affinity for ligand binding^{2,10}. However, the activation of a
39 particular integrin, $\alpha_5\beta_1$ appears to follow a separate mechanism where an extended conformation

Multiscale Integrin Mechanosensing and Cell Adhesion

40 may not be required to bind to its primary ligand, fibronectin (FN)^{11,12}. Instead, $\alpha_5\beta_1$ binds to FN
41 before cytoplasmic proteins anchor it to the cytoskeleton and additional integrins cluster together
42 to create a mature FA (Fig. 1A).

43 The connection between $\alpha_5\beta_1$ integrin and FN is a main mechanosensing unit for external
44 forces transmitting along amino acid residues that mediate cell adhesion¹². The two principal
45 $\alpha_5\beta_1$ binding sites in FN include the 8-amino-acid-long DRVPHSRN synergy site and the RGD
46 motif^{12–14}. Upon mutation of R1374 and R1379 within the synergy site, spinning disk assays
47 showed a reduction in cell-substrate adhesion strength; moreover, a perturbation of FN's RGD
48 motif inhibited adhesion altogether¹⁵. While the synergy site and RGD motif have been shown
49 to play a role in cell adhesion, their nanoscale dynamics and force transduction pathway are less
50 resolved. Elucidating how these residues maintain cell adhesion during integrin mechanosensing
51 is important because their nanomechanics could be leveraged to control cell phenotype or motility.

52 Notably, $\alpha_5\beta_1$'s predominant role in mediating cell adhesion lends itself to be instrumental in
53 the progression of various pathologies. For example, imposing a fibrotic microenvironment on
54 cells by depositing collagen-I or applying biomechanical forces to the cancer cells leads to greater
55 $\alpha_5\beta_1$ integrin-mediated proliferation^{16,17}. Similarly, as a tumor's rigidity increases, mechanosen-
56 sitive $\alpha_5\beta_1$ integrins are recruited and cluster together, creating larger FAs and stress fibers that
57 promote tumor growth via a positive biochemical and biophysical feedback loop^{18,19}. By under-
58 standing the link between nano and micromechanics of the cell, we could influence differentiation
59 or mitigate the uncontrolled spread of metastatic cells through targeted protein or drug design.

60 Therefore, to uncover the mechanical coupling between the nanoscale dynamics of key residues
61 in $\alpha_5\beta_1$ integrin and whole-cell adhesion dynamics, we built a multiscale model. Specifically, we
62 combined adhesion kinetics, the finite element (FE) method, and molecular dynamics (MD) to
63 demonstrate how key residues contributed to spring-like force-extension behavior which in turn
64 influenced the whole-cell spatial distribution of forces on integrins (Fig. 1B). The force per integrin
65 results from our model were within those measured by past atomic force microscopy (AFM)²⁰ and
66 Förster resonance energy transfer (FRET) measurements²¹. The model indicated localization of
67 $\alpha_5\beta_1$ integrin along the cell periphery, which is consistent with cell-based studies that stain for
68 β_1 integrin and FN fragments²². Most importantly, the model contributed an inside look at the
69 molecular dynamics by which the DRVPHSRN synergy site and RGD motif work together to
70 mediate whole-cell adhesion mechanics.

Multiscale Integrin Mechanosensing and Cell Adhesion

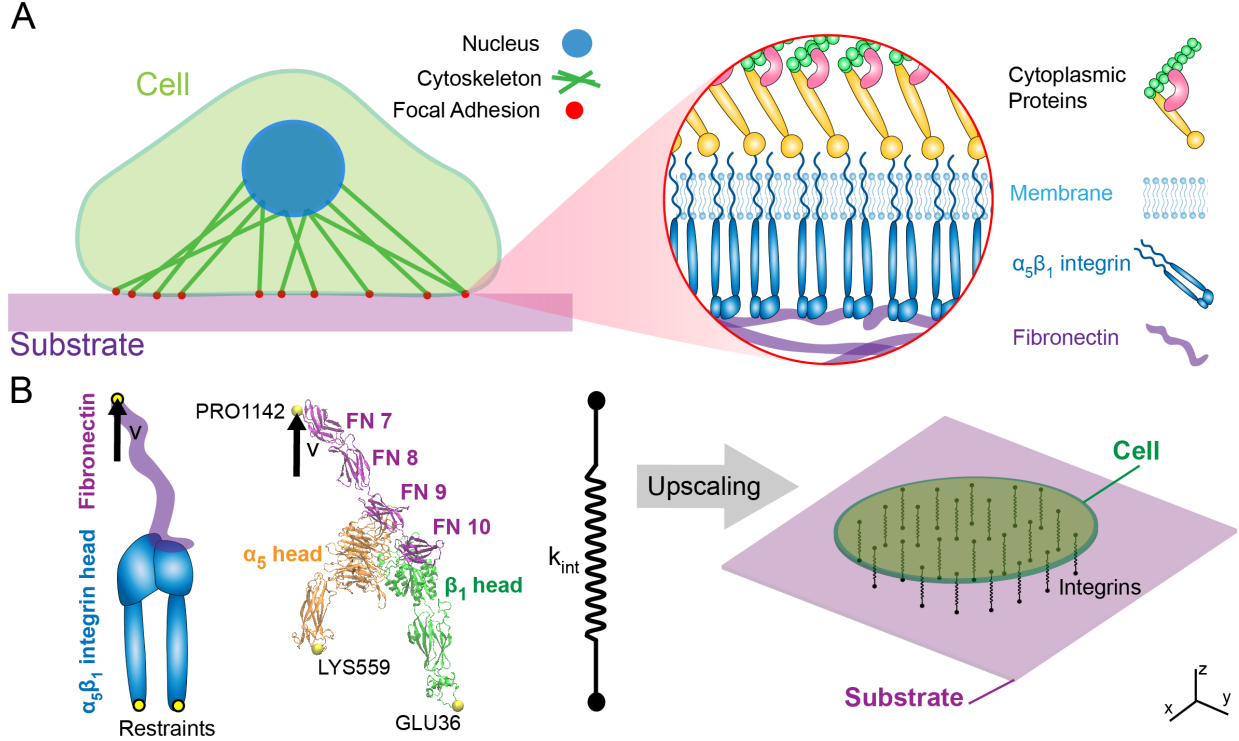


FIG. 1. Simplified schematic of multiscale cell mechanobiology within cell adhesion mediated by $\alpha_5\beta_1$ integrin (A) The cell attaches to a substrate via FAs which house multiple biomolecules including cytoskeletal proteins that anchor integrins to corresponding ligands. (B) The molecular assembly consisted of $\alpha_5\beta_1$ integrin head bound to fibronectin type III fragment 7-10. For the MD simulations, restraints were placed on GLU36 and LYS559 with an applied velocity at PRO1142. The $\alpha_5\beta_1$ -FN's stretching behavior was characterized by a spring that was applied to a 2D continuum model of an elastic cell on a substrate.

71 II. METHODS

72 A. All-atom Steered Molecular Dynamics

73 The 7NWL.pdb file containing human $\alpha_5\beta_1$ integrin in complex with FN and TS2/16 Fv-clasp
 74 was downloaded from the Protein Data Bank¹². Schumacher et al. used the TS2/16 Fv-clasp to aid
 75 in the crystallization of $\alpha_5\beta_1$ -FN and is not naturally occurring and was therefore removed using
 76 PyMOL 2.5²³, leaving three protein chains to be analyzed as part of the remaining complex: α_5
 77 integrin, β_1 integrin, and FN type III. We refer to this complex, or system as " $\alpha_5\beta_1$ -FN."

78 All-atom molecular dynamics (MD) simulations were run in GROMACS 2018.3²⁴ with the
 79 AMBER99SB-ildn force field and periodic boundary conditions. Using the Gromacs built-in func-

Multiscale Integrin Mechanosensing and Cell Adhesion

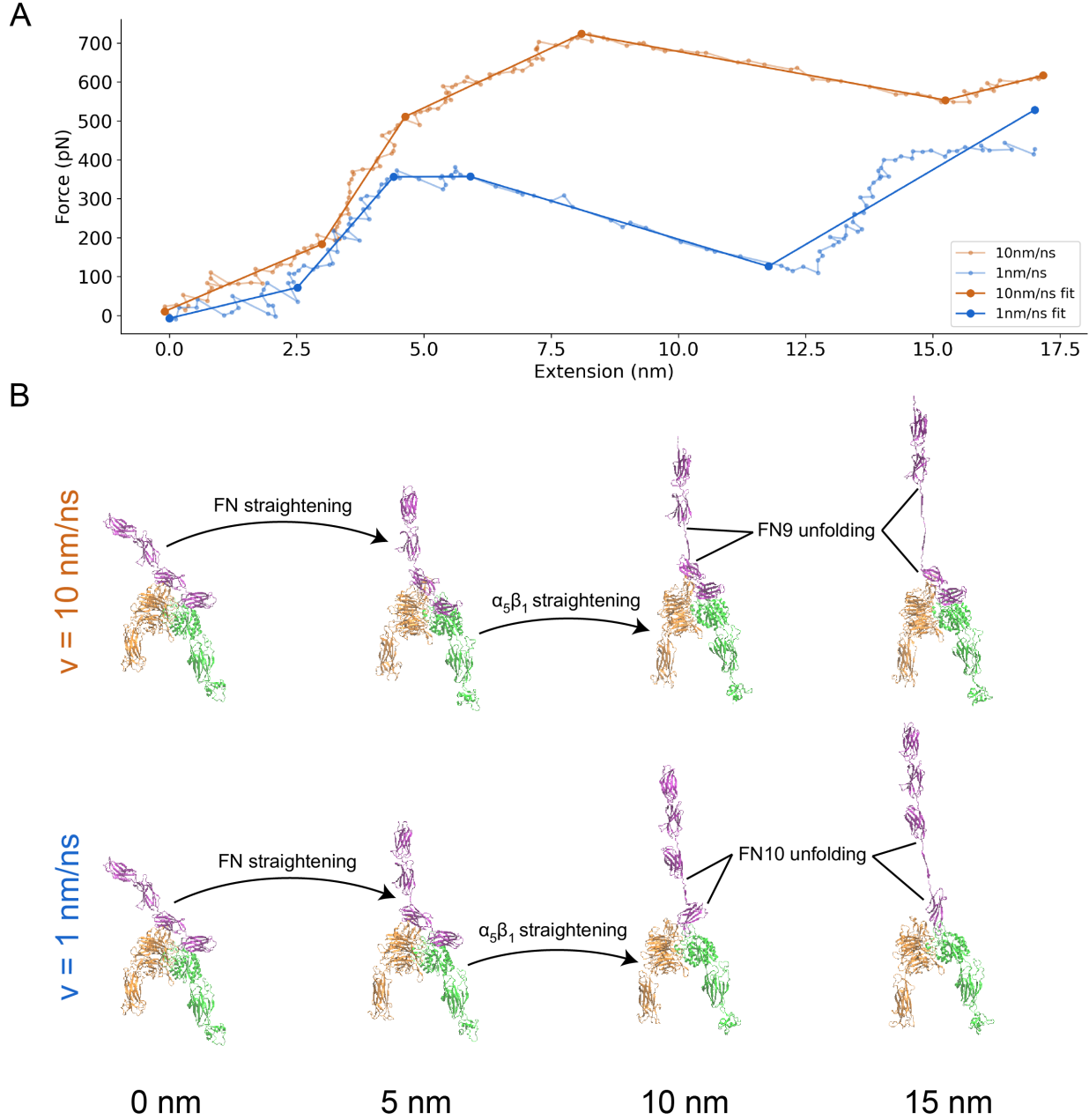


FIG. 2. (A) Force-extension curve of $\alpha_5\beta_1$ -FN stretching at 10 and 1 nm/ns. The raw data are shown in transparent solid lines and the 5-segment piecewise linear fits are shown in opaque solid lines. (B) Frames of $\alpha_5\beta_1$ -FN during extension at 10 nm/ns and 1 nm/ns showing distinct stretching configurations at 0, 5, 10, and 15 nm of extension. In both cases, FN and $\alpha_5\beta_1$ straightened before FN unfolded. However, for the 10 nm/ns case, the FN9 subdomain unfolded. Whereas for the 1 nm/ns case, FN10 unfolded. Movies showing $\alpha_5\beta_1$ -FN extension can be found in the Supplementary Materials.

80 tion, gmx editconf, we rotated the $\alpha_5\beta_1$ -FN complex 45 degrees to align the structure inside a

Multiscale Integrin Mechanosensing and Cell Adhesion

81 18nm x 45nm x 19nm box. The structure was solvated in a TIP3P water box with 0.15mM NaCl
82 resulting in a system with 1.5 million atoms.

83 The energy minimization step was carried out for 15k steps utilizing the steepest gradient
84 descent algorithm with a step size of 0.005nm. Energy over time was extracted using the gmx
85 energy command and then plotted in Python. The structure was then equilibrated using a sequen-
86 tial 1ns NVT followed by a 10ns NPT simulation with H-bonds restrained. For the NVT simu-
87 lation, we used Nose-Hoover temperature coupling at 310K. For the NPT simulation, Parrinello-
88 Rahman pressure coupling at 1 bar was added. After the equilibration runs were completed, we
89 extracted and plotted the root-mean-square deviation (RMSD), temperature, and pressure to con-
90 firm system stability.

91 Upon verifying system equilibration, we ran two steered MD simulations. The positions of
92 Lysine (LYS) 559 and glutamic acid (GLU) 36 at the proximal ends of the integrin headpieces
93 were restrained using the gmx genrestr command (Fig. 1B). Proline (PRO) 1142 at the distal
94 end of the FN chain was pulled vertically at 1 and 10 nm/ns using a 50kJ/mol/nm spring with an
95 umbrella potential for 25 and 3 ns, respectively. Constant force simulations were ran with vertical
96 pulling forces of 300 and 500 pN on PRO1142. The simulations only model the $\alpha_5\beta_1$ integrin
97 headpiece and assume that the lower legs of $\alpha_5\beta_1$ and cell membrane, which are omitted, fix the
98 positions of the headpieces at the proximal end. The model also assumes a completely vertical
99 pulling load stemming from cell and substrate displacement and ignores any shear or rotational
100 loads. The timestep for all steered MD simulations was 2fs. The Molecular Dynamics Parameter
101 (.mdp) files for running the energy minimization, equilibration, and steered MD can be found in
102 the Supplementary Materials. We used the Gromacs built-in function gmx gyrate to measure the
103 radius of gyration of the α_5 and β_1 integrin heads.

104 B. Force Distribution Analysis

105 Protein structures and MD simulation trajectories were visualized in Visual Molecular Dynam-
106 ics (VMD) 1.9.4a²⁵. We then used the Time-Resolved Force Distribution Analysis (FDA) soft-
107 ware package, gromacs-fda (available: <https://github.com/HITS-MBM/gromacs-fda>) with
108 Gromacs 2020.4 to calculate the punctual stresses at each of the residues along the α_5 and β_1 in-
109 tegrin chains, as well as FN. The punctual stress is the sum of absolute values of scalar pairwise
110 forces exerted on each residue. The parameter settings for the FDA can be found in the Supple-

¹¹¹ menary Materials. The gromacs-fda-vmd plugin overlaid the punctual stress heatmap onto the
¹¹² protein renderings in VMD. Areas of interest for the FDA were the DRVPHSRN synergy site and
¹¹³ RGD motif/loop (Fig. 3).

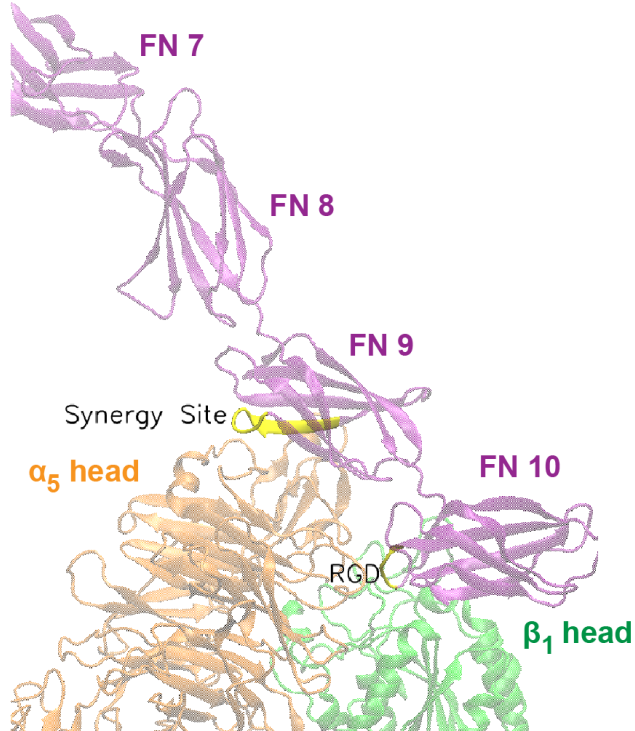


FIG. 3. Close up view of DRVPHSRN synergy site and RGD motif/loop (shown in yellow) in FN that interact with the α_5 and β_1 heads, respectively.

¹¹⁴ **C. Whole-Cell Finite Element Model**

¹¹⁵ The custom finite element (FE) model represented the cell as a thin elastic disk on top of an
¹¹⁶ elastic substrate. The cell surface was assumed to be a neo-Hookean²⁶ constitutive material model.

$$\sigma_s^{\text{pas}} = \mu_s \mathbf{b}_s - p_s \mathbf{I}, \quad (1)$$

$$\sigma_c^{\text{pas}} = \mu_c \mathbf{b}_c - p_c \mathbf{I}, \quad (2)$$

¹¹⁷ where σ_s^{pas} and σ_c^{pas} are the passive substrate and cell stress respectively. The shear moduli
¹¹⁸ are denoted μ_s , μ_c (Table I). The deformation is characterized by the left Cauchy-Green tensors

Multiscale Integrin Mechanosensing and Cell Adhesion

¹¹⁹ **b_s, b_c.** The pressures p_s, p_c are computed from boundary conditions, in this case for plane stress,
¹²⁰ ignoring 3D deformations.

TABLE I. Whole-cell Model Parameter Settings

Parameter	Variable	Setting
Substrate modulus	μ_s	1 MPa
Substrate density	ρ_s	1.0 $\mu\text{g}/\mu\text{m}^3$
Cell modulus	μ_c	1 kPa
Cell density	ρ_s	1000 kg/m ³
Max $\alpha_5\beta_1$ -FN density	$\rho_{i_{max}}$	100 μm^{-2}
Catch-slip bond parameters	K_a	0.004 s^{-1}
	K_b	10 s^{-1}
	F_a	15 pN
	F_b	15 pN

¹²¹ To account for cell contractility, an active stress field was applied inside the cell,

$$\sigma_c^{\text{act}} = t_{\text{myo}} \mathbf{I}, \quad (3)$$

¹²² where σ_c^{act} is the active cell stress due to the applied actin-myosin traction, t_{myo} (Pa):

$$t_{\text{myo}} = \begin{cases} 100t & 0 < t < 2 \\ 200 & 2 \leq t \leq 12 \end{cases} \quad (4)$$

¹²³ where t is the simulation time. We used a previously developed catch-slip bond model of adhesion to determine the number of integrin-substrate bonds per node in the FE mesh in a force dependent manner^{27,28}. This model assumes that the $\alpha_5\beta_1$ -FN complexes behave as parallel springs that connect and disconnect to the substrate based on an association constant, K_{on} and on a force dependent dissociation constant, K_{off} , respectively.

$$K_{off} = K_a e^{\frac{f_{int}}{F_a}} + K_b e^{-\frac{f_{int}}{F_b}}, \quad (5)$$

¹³¹ where K_a, F_a, K_b , and F_b are fitted parameters (Table I) and f_{int} is the magnitude of the force
¹³² per $\alpha_5\beta_1$ -FN bond. The force vector per bond, (\mathbf{f}_{int}), is computed via the $\alpha_5\beta_1$ -FN spring constant
¹³³ k_{int} and the spring extension vector \mathbf{u}_{int} :

134 $\mathbf{f}_{\text{int}} = k_{\text{int}} \mathbf{u}_{\text{int}}.$ (6)

135 The force per node from integrin and is related to the fraction (concentration) of $\alpha_5\beta_1$ -FN bonds
 136 C with respect to the maximum density $\rho_{i,\text{max}}$ (Table I), the local area of the adhesion A (area per
 137 node of the FE mesh), at that node,

138 $\mathbf{f}_{i,\text{node}} = C \rho_{i,\text{max}} A \mathbf{f}_{\text{int}}.$ (7)

139 The fraction of $\alpha_5\beta_1$ -FN bonds C needs to be updated in time. For a given node, i given the pre-
 140 vious value of the bond concentration, C , the updated bond concentration $C_{t+\Delta t}$ at each subsequent
 141 time step is based on the update

142 $C_{t+\Delta t} = C(1 - K_{off}\Delta t) + K_{on}\Delta t(1 - C).$ (8)

143 Note that the update eq. (8) is based on treating the bond kinetics in the limit of an ordinary
 144 differential equation discretized in time with an explicit Euler scheme.

145 The internal force balance for the cell and substrate include elastic deformation of the cell
 146 (σ_c^{pas}), active contractile stress within the cell (σ_c^{act}), and elastic deformation of the substrate
 147 (σ_s^{pas}):

$$\nabla \cdot \boldsymbol{\sigma}_c = \rho_c \mathbf{a}_c \quad (9)$$

$$\nabla \cdot \boldsymbol{\sigma}_s = \rho_s \mathbf{a}_s \quad (10)$$

148 where $\boldsymbol{\sigma}_c = \sigma_c^{\text{pas}} + \sigma_c^{\text{act}}$ is the total stress in the cell, $\boldsymbol{\sigma}_s = \sigma_s^{\text{pas}}$ is the total stress in the substrate,
 149 ρ_c, ρ_s are the densities of cell and substrate respectively (Table I), and $\mathbf{a}_c, \mathbf{a}_s$ the corresponding
 150 accelerations.

151 The strong forms of the elastodynamic equations 9 and 10 have boundary conditions of the form
 152 $\boldsymbol{\sigma} \cdot \mathbf{n} = \mathbf{t}$ on boundary Γ . The strong forms are not directly evaluated. Rather, the internal forces
 153 were computed through the weak form. We multiplied both elastodynamic equations separately
 154 by test function, v , integrated over a domain Ω of thickness $1\mu\text{m}$, and applied divergence theorem
 155 to get the following weak form for the cell (subscript c) and substrate (subscript s), respectively.

$$-\int_{\Omega_c} \sigma_c : \delta \mathbf{d}_c d\Omega_c + \int_{\Gamma_c} \mathbf{t}_c \cdot \delta \mathbf{v}_c dA_c = -\mathbf{R}_c + \mathbf{f}_{c,ext} = \int_{\Omega_c} \rho \mathbf{a}_c d\Omega_c \quad (11)$$

$$-\int_{\Omega_s} \sigma_s : \delta \mathbf{d}_s d\Omega_s + \int_{\Gamma_s} \mathbf{t}_s \cdot \delta \mathbf{v}_s dA_s = -\mathbf{R}_s + \mathbf{f}_{s,ext} = \int_{\Omega_s} \rho \mathbf{a}_s d\Omega_s \quad (12)$$

The $\delta \mathbf{d}$ is the variation of the symmetric velocity gradient, i.e. virtual work by moving each node by an independent variation $\delta \mathbf{v}$. \mathbf{R} is the residual and the external force acting at a particular node of the respective cell and substrate meshes is:

$$\mathbf{f}_{c,ext} = \mathbf{f}_{i,node} + \mathbf{f}_d + \mathbf{f}_K + \mathbf{f}_{ac} + \mathbf{f}_A \quad (13)$$

$$\mathbf{f}_{s,ext} = -\mathbf{f}_{i,node} + \mathbf{f}_d \quad (14)$$

where $\mathbf{f}_{i,node}$ is the force due to integrin at each node, \mathbf{f}_d is viscous drag, \mathbf{f}_K is curvature regularization, \mathbf{f}_{ac} is a random fluctuation at the cell boundary from actin polymerization, and \mathbf{f}_A is an area penalty to counteract cell contractility. Note that the nodal integrin force acts on the cell and substrate surfaces in opposite directions. The remaining variables act on the cell border and are further explained in the Supplementary Materials.

A dynamic explicit mesh generator, El Topo²⁹, created and maintained the mesh during the simulation run. The explicit mid-point rule was used for time integration of the second order system of equations to update nodal velocities and positions. Three $\alpha_5\beta_1$ -FN stiffness values (k_{int}) were used: 1pN/nm, 31pN/nm, and variable stiffnesses extracted from the MD simulation force-extension curves (MD-driven). The variable stiffness of the $\alpha_5\beta_1$ -FN complex within the FE model was modeled as a nonlinear spring by applying piece-wise linear interpolation in Python to the force-extension curves provided by the MD simulations as described in Section II D. Settings for each simulation run can be found in Supplementary Materials.

The overall sequence of the multiscale model is summarized in Figure 4. To summarize, the whole-cell FE model first imports the cell and substrate meshes and calculates the velocities and positions of the nodes. The $\alpha_5\beta_1$ -FN bonds are spread out uniformly across the surface of the cell with bond attachment points on the cell and the substrate. The displacement between the cell and substrate attachment points dictate the bond stretch. For the MD-driven case, the bond stiffness, k_{int} is assigned based on the bond stretch. Otherwise, the stiffness is directly assigned according to each constant case ($k_{int}=1$ or 31 pN/nm). The force per bond is then calculated via Hooke's

179 Law (eq. 6). This force is then used to update two things: the force per node (eq. 7) and the bond
180 kinetics (eqs. 5 and 8). Cell contraction (eqs. 3 and 4) is then applied and the residual is computed
181 via the weak form (eq. 11 and 12) considering the cell and substrate respective material properties
182 (eq. 1 and 2), their elastodynamics (eqs. 9 and 10), and their force balances (eqs. 13 and 14). The
183 nodal strains, velocities, and positions are updated and lastly, the simulation frame is saved. The
184 whole-cell FE simulation iterates with a 1000-element mesh and a timestep of $dt = 50\mu s$ over the
185 course of an assigned time, $t_{sim} = 12s$. Mesh and timestep convergence data can be found in the
186 Supplementary Materials.

187 **D. Multiscale Model Coupling**

188 The Gromacs function, mdrun outputted the force on the $\alpha_5\beta_1$ -FN complex. Furthermore, gmx
189 trajectory was used to extract the center-of-mass coordinates of the restraints, LYS559 and
190 GLU36, as well as the pull residue, PRO1142. The $\alpha_5\beta_1$ -FN extension length was measured in
191 Python as the average vertical distance between PRO1142 and each of the two restrained residues.
192 The resulting force-extension curve for each simulation run was then plotted. The optimize
193 function from the SciPy library was used to produce a 5-segment piecewise linear fit on the 1
194 and 10 nm/ns force-extension curves, respectively. Ultimately, the 1 nm/ns curve-fit was used as
195 a variable displacement-dependent spring constant in the whole-cell model to make up the "MD-
196 driven" $\alpha_5\beta_1$ -FN stiffness, k_{int} .

197 **III. RESULTS AND DISCUSSION**

198 **A. $\alpha_5\beta_1$ -FN exhibited nonlinear and rate dependent stretching behavior under applied
199 constant velocity**

200 Prior to running the steered MD simulations at two pulling rates, the model's energy minimized
201 to -1.37e7 kJ/mol and the RMSD of the system plateaued while the pressure and temperature also
202 remained stable during the NPT simulation (Supplementary Material). We chose 1 and 10 nm/ns
203 pull rates for the steered MD simulations based on similar rates in other integrin subtypes^{30,31}.
204 As expected, $\alpha_5\beta_1$ -FN exhibited rate-dependent stretching behavior, meaning that the $\alpha_5\beta_1$ -FN
205 force-displacement curves varied by pull rate (Fig. 2 A). The 10 nm/ns simulation reached a
206 higher peak force of 723 pN and greater initial slope of 56 pN/nm compared to 444 pN and 31

Multiscale Integrin Mechanosensing and Cell Adhesion

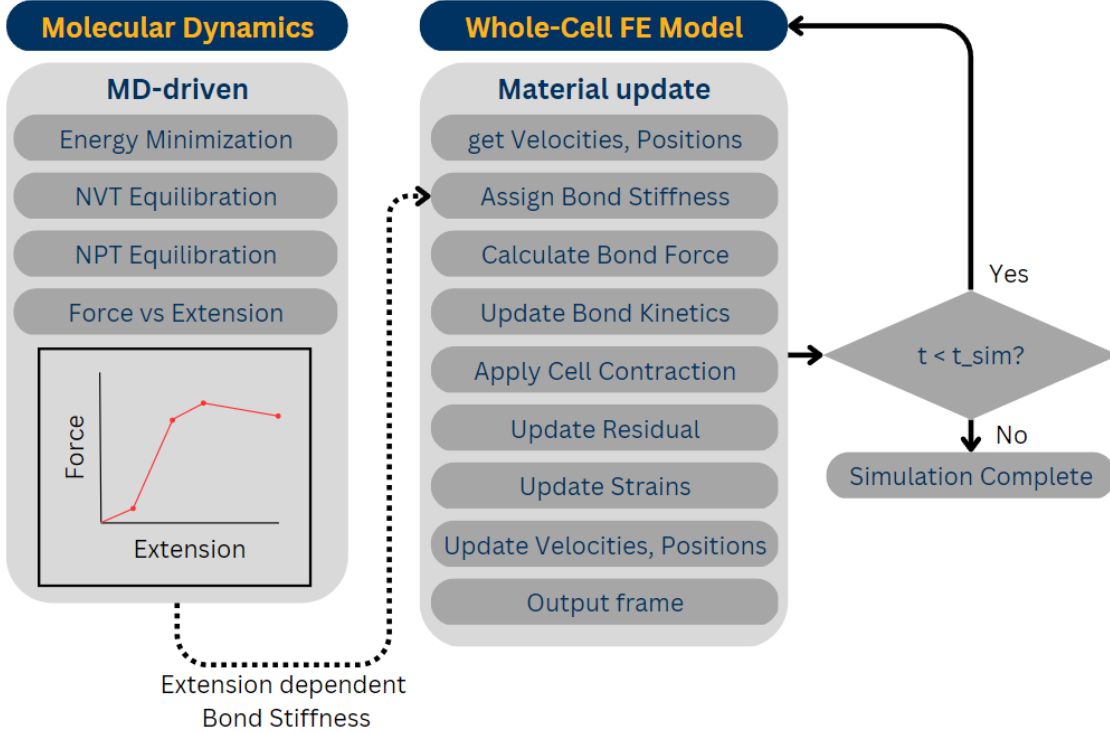


FIG. 4. Multiscale framework that links the MD model to the FE model via a variable spring constant.

207 pN/nm, respectively for the 1 nm/ns simulation.

208 In both cases, the stretching was dominated by FN, while integrin remained mostly rigid with
 209 some minor rotation and straightening. Curiously, at the faster 10 nm/ns pull rate, FN9 unrav-
 210 eled first before unbinding from the α_5 head at the synergy site, whereas limited unraveling of
 211 FN was observed prior to unbinding for the slower 1 nm/ns pull rate (Fig. 2 B). Following the
 212 disconnection between FN and α_5 at the synergy site, the force on the whole $\alpha_5\beta_1$ integrin head
 213 became biased towards the RGD motif, causing the integrin heads to straighten with elongation
 214 of α_5 and β_1 . However, the degree of head straightening was not consistent for both pull rates
 215 over the course of $\alpha_5\beta_1$ -FN extension. We opted to use radius of gyration (R_g) as a proxy for
 216 integrin head straightness, with a larger radius indicating a straighter head. Visually, each integrin
 217 head started in a more closed positions with a relatively small R_g before opening. Therefore, we
 218 believed it was appropriate to assume that a larger R_g corresponded to a straighter molecule. For
 219 both rates, we observed an initial increase in the R_g of both integrin heads prior to the unbinding
 220 of the salt bridge between arginine (ARG) 1379 in FN9 and aspartic acid (ASP) 154 in α_5 (Fig.
 221 5). However, the faster rate showed a sharp increase in R_g of both heads after the salt bridge break
 222 at 6.1 nm, indicative of additional bonds pinning FN9 to α_5 that then led to FN9 unfolding and α_5

and β_1 head straightening. In contrast, at the slower rate, we noticed a steady decrease in R_g of both heads as FN10 unfolded immediately after the ARG1379-ASP154 break at 5.7 nm, presumably because α_5 was allowed to relax after the departure of FN9. The faster rate elicits a greater reaction force out of $\alpha_5\beta_1$ -FN, which were resisted by other bonds between FN9 and α_5 and a straightening of the integrin heads. This result was notable because it provided insight into how integrin may exhibit increased bond lifetime at higher forces, characteristic of previously observed catch bond behavior of integrins^{15,32}.

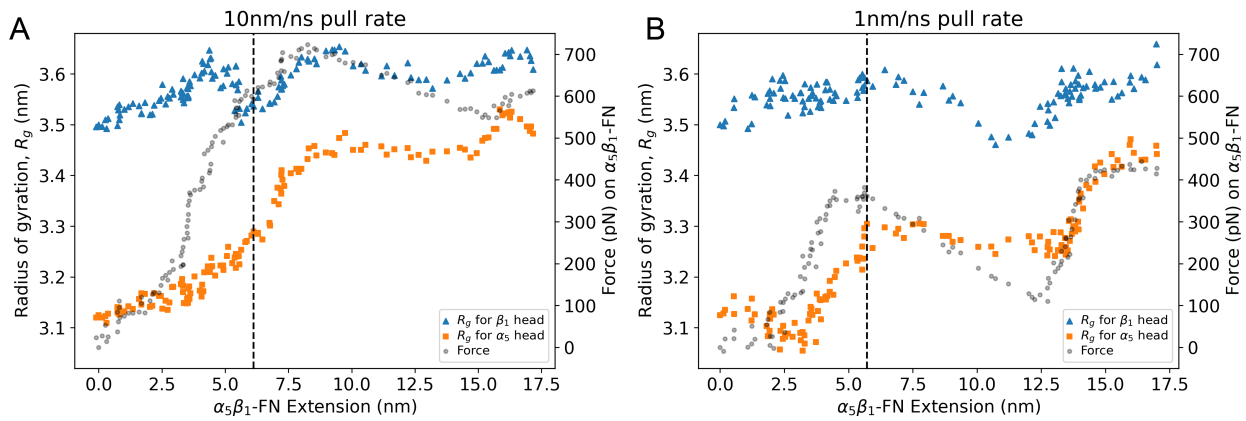


FIG. 5. Radius of gyration (left vertical axis) of α_5 and β_1 heads and force (right vertical axis) on $\alpha_5\beta_1$ -FN during A) 10 nm/ns and B) 1 nm/ns extension. The dashed vertical line on each plot represents the moment the ARG1379-ASP154 salt bridge was broken.

The observed viscoelastic behavior of $\alpha_5\beta_1$ has been shown both experimentally and computationally. Single-molecule AFM studies show higher rupture forces at faster pull rates²⁰ and separate steered MD simulations of integrin^{30,31} and FN³³ showed rate-dependent and force-dependent stretching behavior seen in viscoelastic materials. We expected this viscoelastic behavior to remain when $\alpha_5\beta_1$ and FN are in complex. To confirm, we tested $\alpha_5\beta_1$ -FN's viscoelasticity *in silico* via constant force simulations at 300 and 500 pN, similar to what would be done in a mechanical creep test where constant stress is applied (Fig. 6). We fit the Bausch viscoelasticity model, which combines a Kelvin model with a dashpot in series³⁴, to the extension-time plots, supporting the characterization of $\alpha_5\beta_1$ -FN's time-dependent stretching and viscoelastic nature.

While our MD simulations and previous literature have demonstrated the nonlinear stretching behavior of $\alpha_5\beta_1$ -FN, multiscale models assume a linear integrin stiffness between 0.001-2 pN/nm^{27,28,35}. Recent multiscale models have used this assumption when analyzing fundamental phenomena such as integrin activation, organization, and clustering at the cell and tissue

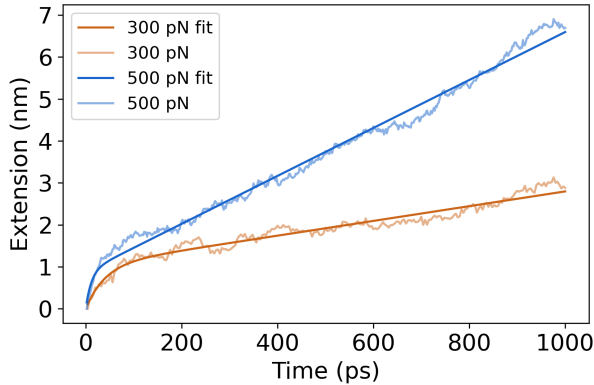


FIG. 6. Extension plots of constant force simulations at 300pN and 500pN pulling forces. The Bausch³⁴ viscoelastic model was fit to each of the plots.

scales^{27,28,35}. Most recently, Guo et al. showed a framework that combined adhesion kinetics with the finite element method (FEM) to model stretch-driven mechanosensing at the tissue level by coupling integrin adhesion with the nonlinear tissue mechanics of fibrin and collagen²⁷. While these models provide unique insights into multiscale mechanobiology of cell adhesion, for models to account for integrin and FN's nonlinear stretching behavior, a dynamic spring stiffness that adjusts depending on extension is required. For our work, we used our steered MD force-extension plots to inform a dynamically changing spring in a continuum model of the whole cell.

A limitation of our approach is that MD simulations are computationally expensive and run-times would be unreasonably long if we adopted experimentally relevant 800 nm/s pull rates used by past AFM studies^{36,37}. However, using faster pull rates leads to higher single-molecule forces beyond 300pN as was noticed in our force-extension curves. Moreover, the MD model limited the flexibility of the proximal ends of the integrin heads by restraining them with a harmonic spring, potentially contributing to larger measured forces. The heads may have otherwise been more free to move depending on the motion of the integrin legs and tails within the cell membrane, which were not modeled to reduce computational cost and add model stability. Previous studies found average *in situ* rupture forces for $\alpha_5\beta_1$ -FN to be 34³⁶ and 38.6 pN³⁷ in endothelial cells and cardiomyocytes, respectively. Single molecule AFM conducted by Li et al. measured a mean rupture force of $\alpha_5\beta_1$ -FN of 69 pN at a loading rate of 1800-2000 pN/s, with a peak rupture force of 120 pN at 18,000 pN/s²⁰. More recently, FRET-based sensors were used to measure adhesion forces between 1-7 pN on fibroblasts plated on glass²¹. All these measured forces are much lower than those predicted by the MD simulations. Higher forces at much faster pull rates meant

Multiscale Integrin Mechanosensing and Cell Adhesion

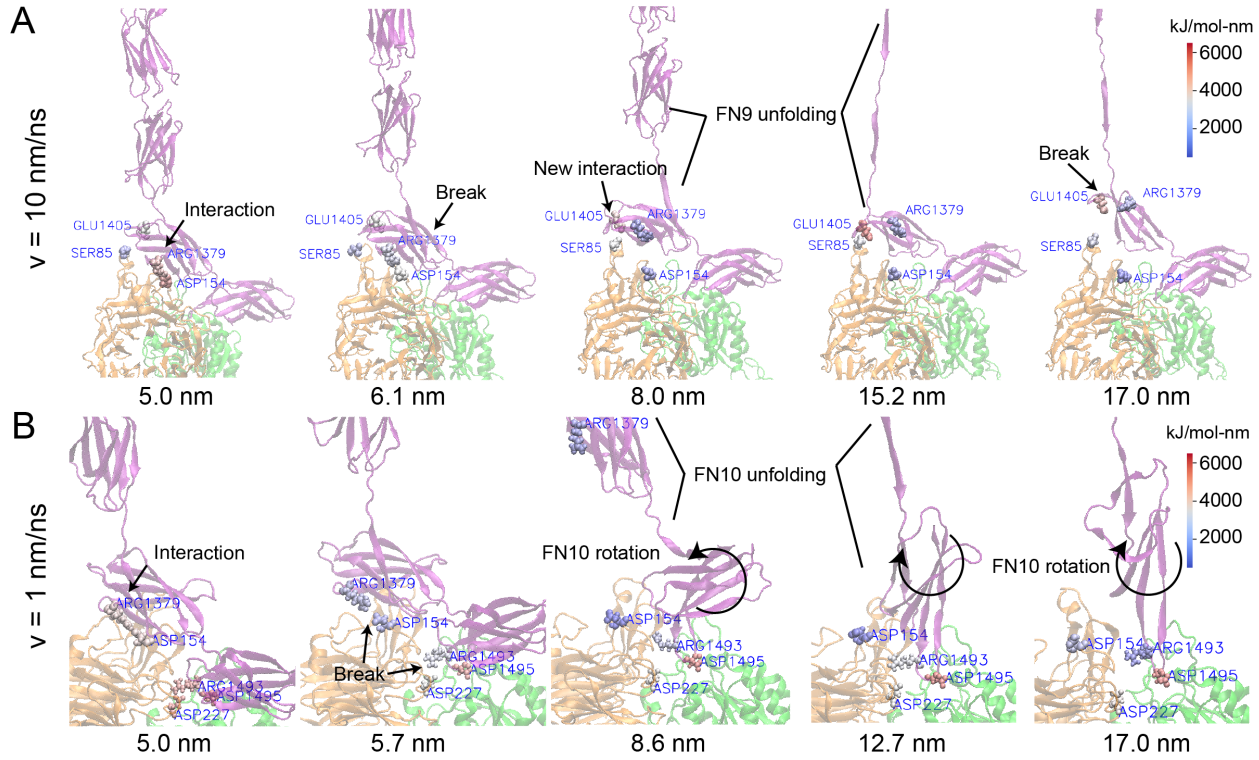


FIG. 7. Force Distribution Analysis of $\alpha_5\beta_1$ -FN for two pull rates at key events. The color map refers to the punctual stress (in kJ/mol-nm) at each residue. (A) At 10 nm/ns, there was a coulombic interaction at the ARG1379-ASP154 salt bridge and no interaction between GLU1405 and SER85. As FN was extended, the salt bridge ruptured and allowed FN to rotate and establish a new interaction between GLU1405 and SER85. FN9 continued to unfold, increasing stress on the GLU1405-SER85 connection, eventually breaking it. (B) At 1 nm/ns, the ARG1379-ASP154 salt bridge, part of the synergy site, together with ARG1493 and ARG1495, part of the RGD motif, maintained a hold on FN. As FN extended, increased stress led to the simultaneous rupture of ARG1493-ASP227 and ARG1379-ASP154. This allowed FN10 to unfold and rotate. ARG1493-ASP227 disconnected and reconnected throughout the remainder of the simulation. Movies showing the FDA can be found in the Supplementary Materials.

that our $\alpha_5\beta_1$ -FN stiffness results were significantly larger than what has been observed *in vitro*. However, in all the experiments, the nonlinearity of $\alpha_5\beta_1$ -FN's stretching behavior was apparent, challenging the linear stiffness assumption made by previous models^{27,28,35}. Furthermore, while an average FN stiffness of 0.5 pN/nm has been reported^{38,39}, the coupled $\alpha_5\beta_1$ -FN stiffness has not. Additionally, our steered MD simulations provided atomic level details that helped explain how key binding sites contributed to pull rate dependent nonlinear stretching.

270 **B. Force Distribution Analysis of $\alpha_5\beta_1$ -FN reveals dynamics of adhesion-mediating
271 residues that contribute to nonlinear force-extension behavior**

272 Visualization of the coulombic interactions via Force Distribution Analysis of the steered MD
273 results demonstrated how key adhesion mediators could contribute to nonlinear, rate-dependent,
274 force-extension of $\alpha_5\beta_1$ -FN. Two key mediators are the DRVPHSRN synergy site and the RGD
275 motif in FN (Fig. 3). In our system, the FN synergy site was represented by residues 1373 to 1380
276 and the RGD motif was represented by residues 1493 to 1495. Spinning disk microscopy has
277 previously shown that mutating one to two select residues on the synergy site leads to a decrease
278 in overall cell adhesion and mutating the RGD motif eliminates cell adhesion force completely¹⁵.
279 Furthermore, inducing a synergy site mutation or an RGD deletion leads to a reduction in single
280 molecule rupture force of $\alpha_5\beta_1$ -FN²⁰. Therefore, we looked closely at the dynamics of these
281 adhesion mediators during $\alpha_5\beta_1$ -FN stretching at 1 nm/ns and 10 nm/ns.

282 Interestingly, the $\alpha_5\beta_1$ -FN extension showed two modes of stretching depending on the pull
283 rate. Heatmaps overlaid on the molecule illustrated the degree of coulombic interaction, where
284 "hotter" or "redder" zones indicated larger pairwise punctual stresses. For the 10 nm/ns case,
285 the ARG1379-ASP154 salt bridge is broken after 6.1 nm of $\alpha_5\beta_1$ -FN extension (Fig. 7A). This
286 action then loosens the grip between α_5 and FN9, allowing FN9 to rotate to find a new interaction
287 between glutamic acid (GLU) 1405 and serine (SER) 85. FN9 then unfolded, contributing to the
288 initial decrease in force and most of the extension before GLU1405 and SER85 release. Between 0
289 and 5 nm, FN began to straighten while simultaneously tugging on the synergy site and RGD. The
290 force-extension response "softened" as the salt bridge was broken and FN9 started to rotate. The
291 large extension and reduction in force past 8 nm (Fig. 2) was due to the rapid unfolding of FN9
292 while GLU1405-SER85 pinned the rest of FN9 in place. After two strands of FN9 are unwound,
293 the applied load became directed at the GLU1405-SER85 pin until it finally separated. Notably,
294 the unfolding pathway with two strands unwound of FN9 has been illustrated before in constant
295 force simulations of FN³³. Our model corroborates these results while providing new insight into
296 the dynamics of FN unfolding when interacting with $\alpha_5\beta_1$ integrin.

297 The observed unbinding and unfolding sequence in $\alpha_5\beta_1$ -FN was not preserved at 1 nm/ns.
298 The salt bridges, ARG1379-ASP154 and ARG1493-ASP227 simultaneously broke at 5.7 nm of
299 extension after a short force plateau between 4.8-5.7nm, but unlike in the 10nm/ns run, FN9 did
300 not create a new interaction with α_5 (Fig. 7B). Rather, FN10 unfolded, leading to the majority of

Multiscale Integrin Mechanosensing and Cell Adhesion

301 the overall extension and reduction in force from 5.7-12.7nm (Fig. 2A). During FN10 unfolding,
302 the interaction between ARG1493 in FN and ASP227 in α_5 alternated between high and low
303 coulombic interactions while ARG1495 maintained adhesion with β_1 integrin. Due to the lack
304 of interaction between the synergy site in FN9 and α_5 , FN9 was free to separate from integrin
305 so FN10 could readily unfold. Once one strand had completely unfolded, due to the direction of
306 the pulling force with respect to the orientation of FN10, the force needed to rotate FN10 prior to
307 unwinding the second strand, which led to an increase in force (Fig. 2B).

308 At both pull rates, the synergy site and RGD loop played key roles in maintaining the adhesion
309 between $\alpha_5\beta_1$ and FN. Specifically, the salt bridge between ARG1379 and ASP154 contributed to
310 the molecule's initial "stiff" behavior prior to FN unfolding; and part of the RGD loop between β_1
311 and FN10 was the only remaining connection between integrin and FN after full extension. Due to
312 their instrumental role, it stands to reason that interfering with these residues via point mutations
313 would reduce adhesion¹⁵ and rupture force²⁰. While measured *in vitro* forces on $\alpha_5\beta_1$ -FN have
314 been shown to be much smaller than we have presented due to our model's much faster pulling
315 speed, nonlinear force-extension behavior and rapid jumps in force have been observed^{15,20,21}.
316 We showed how key residues could contribute to this characteristic behavior during $\alpha_5\beta_1$ -FN
317 extension in a pull rate dependent manner. To bridge the nanoscale integrin stretching to cell-scale
318 integrin dynamics, as a proof-of-concept, we modeled the force-extension of $\alpha_5\beta_1$ as a nonlinear
319 spring and used it to scale up to a 2D whole-cell continuum model.

320 C. Multiscale integration of $\alpha_5\beta_1$ -FN force-extension with whole-cell integrin dynamics

321 Prior to integrating the force-extension curves from the MD runs, we had ran a baseline simula-
322 tion of the whole-cell model with similar parameters to those commonly used in literature^{27,28,35}.
323 In particular, we set the $\alpha_5\beta_1$ -FN stiffness, k_{int} , to 1pN/nm. For all simulations, the cell contrac-
324 tility was ramped from 0 to 200Pa within the first 2s and held at 200Pa for the remainder of the
325 12s simulation. Integrins were recruited to the cell border, achieving maximum concentration and
326 force as the contractility reached 200Pa at 2s (Fig. 8).

327 Integrin's spatial distribution on the cell's leading edge during motion has been previously
328 observed *in vitro*²², corroborating the results from the model. During contraction, the model's
329 average peak bond concentration reached 10.6% (Fig. 9A) with a max peak of 22.5%. The average
330 force per bond followed a similar curve, reaching an average peak of 1.9pN (Fig. 9B) with a max

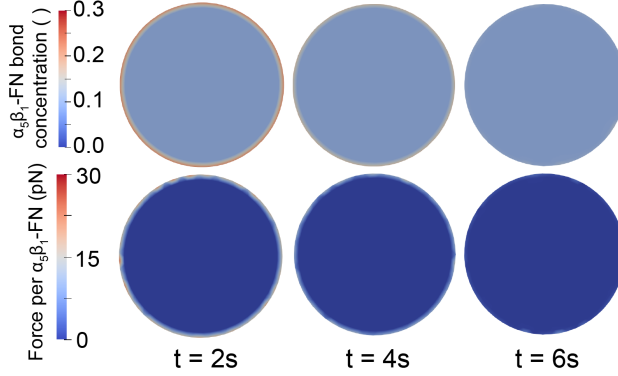


FIG. 8. The dimensionless $\alpha_5\beta_1$ -FN bond concentration (top) and force per $\alpha_5\beta_1$ -FN (bottom) results for the baseline whole-cell simulation with $k_{int} = 1\text{pN/nm}$. $\alpha_5\beta_1$ -FN localization and force dissipation occurred rapidly and no significant changes in distribution were observed past 6s. Movies showing simulation trajectories can be found in the Supplementary Materials.

331 peak of 28.6pN at the cell boundary. These bonds had short lifetimes and dissociated quickly,
 332 allowing the model to dissipate the contraction and reach equilibrium just before the 6s mark.
 333 After reaching this equilibrium point, the mean force was $0.17 \pm 0.04\text{pN}$ with max forces reaching
 334 15.9pN at the boundary. The peak bond forces and concentrations occurred on the boundary due
 335 to the positive feedback loop of the catch-slip bond dynamics. While the strain across the cell
 336 is uniform due to the applied isotropic contractility, the deformation of the bond springs are the
 337 greatest at the boundary, leading to higher bond concentrations and forces. Overall, the forces
 338 were within the 1-38pN range that has been observed *in vitro*^{21,36,37} and well within the peak
 339 single $\alpha_5\beta_1$ -FN rupture forces measured via AFM of 120pN²⁰.

340 The baseline simulation provided a control to test against our two simulation conditions derived
 341 from the 1 nm/ns MD simulation. We defined a varying, MD-driven $\alpha_5\beta_1$ -FN stiffness as the entire
 342 1nm/ns force-extension curve fit. To evaluate how the nonlinearity of the MD-driven integrin
 343 spring affected whole-cell adhesion dynamics, we used the slope of the first segment, 31pN/nm,
 344 to define a constant $\alpha_5\beta_1$ -FN stiffness test condition.

345 Overall, the $\alpha_5\beta_1$ -FN bond concentration for the constant and MD-driven $\alpha_5\beta_1$ -FN stiffness
 346 conditions followed a similar trend and were both slower to distribute the contraction load (Fig. 9)
 347 than the 1pN stiffness setting. Past 2s, the mean forces steadied at $2.45 \pm 0.18\text{pN}$ and $2.59 \pm 0.19\text{pN}$
 348 for the constant and MD-driven runs, respectively. The noise in the the bond concentrations and
 349 force per bond (Fig. 9) were due to the random 5pN actin polymerization force. The results for

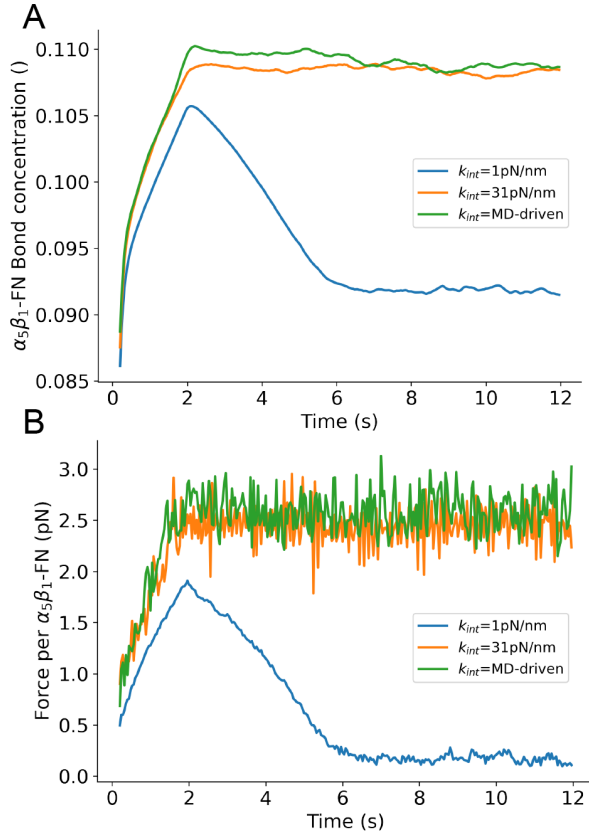


FIG. 9. Whole-cell average A) $\alpha_5\beta_1$ -FN bond concentration (dimensionless) and B) force per $\alpha_5\beta_1$ -FN over the simulation run. Three test conditions for $\alpha_5\beta_1$ -FN stiffness are shown per plot: 1) constant 1pN/nm baseline from past models^{27,28,35}, 2) constant 31pN/nm based on the first segment of the 1nm/ns force-extension curve fit, and 3) MD-driven stiffness derived from using all segments of the curve fit.

both cases were similar. The constant 31pN/nm run reached a max average bond concentration of 10.9% and the MD-driven case topped at 11.0%. Max average forces, located at the cell boundary (Fig. 10), were 53.5pN and 55.6pN for the 31pN/nm and MD-driven runs, respectively. The positive feedback loop of the catch-slip bond at the boundary continued to drive the peak forces and concentrations across all stiffness settings.

Notably, model predictions surpass *in situ* rupture forces of 34-38.6pN for $\alpha_5\beta_1$ -FN^{36,37} and 40pN for another subtype, $\alpha_V\beta_3$ ⁴⁰. Chang et al. used FRET-based sensors to measure adhesion forces between 1-7 pN on fibroblasts²¹. Recent work has used leveraged tension gauge tethers to measure single molecule forces on RGD-binding integrins and showed that integrin activation occurs below 12 pN and $\alpha_V\beta_1$ could sustain forces over 54pN in mature FAs⁴¹. In summary, the models we presented showed estimations towards the upper bounds of measured biophysical

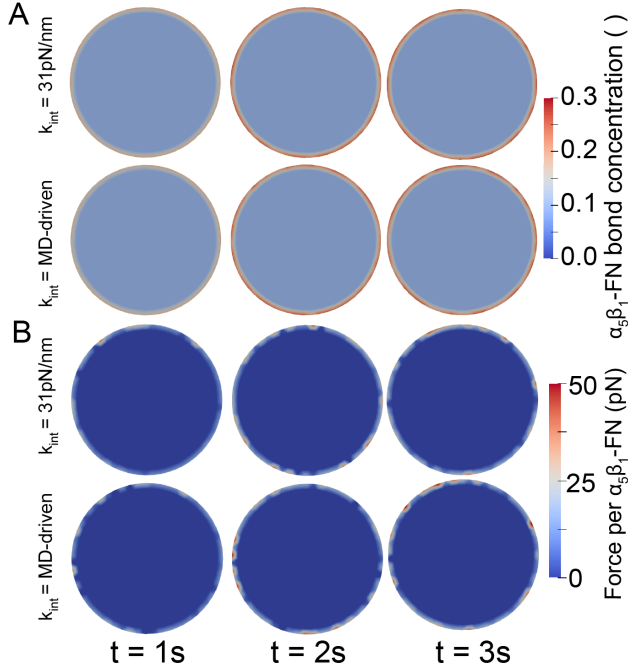


FIG. 10. Whole-cell simulation results for the constant and MD-driven spring stiffnesses. A) $\alpha_5\beta_1$ -FN bond concentration and B) Force per $\alpha_5\beta_1$ integrin at three time frames within the first 3s of the simulation. Dissipation continued past 3s, but the changes were minor. Movies showing simulations can be found in the Supplementary Materials.

³⁶¹ forces felt by integrin.

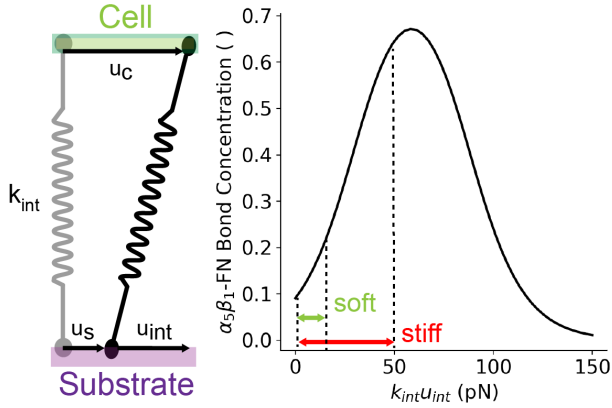


FIG. 11. Schematic of the balance at an equilibrium state between the cell, substrate, and spring deformations contribute to changing bond concentrations based on the catch-slip bond curve (eq. 8).

³⁶² The MD-driven and constant 31pN/nm integrin stiffness models showed similar force and con-
³⁶³ centration results indicating that linear spring stiffness was sufficient to capture $\alpha_5\beta_1$ -FN molec-

Multiscale Integrin Mechanosensing and Cell Adhesion

ular dynamics in this model. Notably, bond lengths were maintained below 2.5nm, where the stiffness jumps to 99.5pN/nm in the MD-driven force-extension curve (Fig. 2A). The main difference observed in the bond force and concentration response was between soft (1pN/nm) and stiff (31pN/nm, MD-driven) integrin models. These differences arose due to the force balance between the cell, the substrate, the integrin, and other random forces (eq. 13). All these forces contributed to the integrin deformation, u_{int} (Fig. 11), which was multiplied by integrin stiffness to calculate force. This bond concentration was updated based on this bond force and catch-slip bond model (Fig. 11 and eq. 8). In our case, the bond lengths ranged from 0-15.9nm for the soft integrin and 0-1.8nm in the stiff integrin. This led to forces between 0-15.9pN and 0-55.6pN for the soft and stiff integrin, respectively. To summarize, the balance between applied forces, cell/substrate material properties, and integrin stiffness led to varying bond deformation which contributed to alterations in bond concentration due to catch-slip bond dynamics.

IV. CONCLUSION

We developed a coupled multiscale model which showed how amino acid interactions at the synergy site in FN contribute to the nonlinear force-extension behavior of $\alpha_5\beta_1$ -FN, which leads to unique whole-cell adhesion force landscapes. The model demonstrated whole-cell integrin spatial distribution along the cell membrane, consistent with fibroblasts plated *in vitro*²² and forces within the 120pN maximum single molecule rupture force and 1-38 pN *in situ* rupture forces^{21,36,37}.

This study has limitations. We used high pull rates in the MD simulations to maintain reasonable computational runtimes. However, this led to large forces during $\alpha_5\beta_1$ -FN extension. While the computational cost is a common drawback of MD, the detailed data and outputs gained from the amino acid dynamics and their connection to whole-cell integrin dynamics would have been otherwise unobservable. Therefore, we believe that it was useful to include this demanding piece of the multiscale model. A combination of slower pull rates and coarse grained MD simulations could be the compromise necessary to investigate the nonlinear mechanics while maintaining some nanoscale details.

Also, we chose $\alpha_5\beta_1$ integrin as the sole surface receptor, but cells have additional subtypes with varying roles^{35,42} and potentially different adhesion strengths⁴¹ and binding kinetics^{43,44}. Given the 24 known subtypes of integrin⁴⁵, it is critical to understand which ones are the main contributors to adhesion maintenance in the presence of specific ligands. For example, in the case

Multiscale Integrin Mechanosensing and Cell Adhesion

394 of fibronectin, a recent single-cell force spectroscopy study indicated that pan integrin knockout
395 fibroblasts only expressing $\alpha_5\beta_1$ and $\alpha_V\beta_3$ transmitted the same amount adhesive force as wildtype
396 fibroblasts on a fibronectin coated surface⁴⁶. Therefore, extending our model to contain these
397 two subtypes may be an appropriate approximation to evaluate integrin adhesion mechanics for
398 fibroblasts on fibronectin. Another key consideration is the dynamics of low-affinity and high-
399 affinity conformations of integrin. For our model, we assumed that $\alpha_5\beta_1$ integrin was in a high
400 affinity, extended-open conformation. However, it has been demonstrated that low-affinity bent-
401 closed and extended-closed conformations of $\alpha_5\beta_1$ and $\alpha_V\beta_3$ can still bind to fibronectin^{44,47}.
402 To include the contributions of varying subtypes, it would be necessary to update to our catch-
403 slip bond model (Fig. 11) to include high and low affinity conformational states, manage the
404 population distribution of integrin subtypes as done in other models^{28,35}, and expand on existing
405 steered MD characterizations of $\alpha_V\beta_3$ ^{30,48} to add to ours of $\alpha_5\beta_1$. Overall, more investigation is
406 needed to evaluate how integrin subtypes collaborate to manage cell adhesion dynamics.

407 The model assumed a homogeneous substrate. However, tissue microenvironments are spatially
408 heterogeneous and respond to the binding and unbinding dynamics between ECM fibers^{49–53}. This
409 leads to viscoplastic material behavior, or time and frequency dependent force dissipation⁵⁴ which
410 mediates cell migration, differentiation, and disease progression^{55–57}. To include these effects, we
411 could represent the substrate viscoplasticity via the Norton-Hoff constitutive model^{49,58}, and the
412 cell's myosin-actin engagement via the molecular or motor clutch model^{53,59}. We would expect
413 a heterogeneity to arise in the force and spatial distribution of the integrin bonds, localizing near
414 denser packs of crosslinked fibers. We hypothesize that stiffer integrins would lead to denser pack-
415 ing of ECM fibers due to their slow rate of sustained force compared to softer bonds. However,
416 more investigation is needed to reveal the relationship between cell adhesion and force-mediated
417 ECM fiber mechanics.

418 Our model focused on cell adhesion mechanics and has the potential to grow into a frame-
419 work that can investigate cell mechanotransduction across multiple scales. For example, we could
420 test how unique mutations on integrins affect whole-cell dynamics *in silico*. Additionally, by in-
421 corporating the cell nucleus, we could support early evidence to show how its mechanosensitive
422 nature and material properties could govern gene transcription^{60–62}. Key components that have
423 previously been modeled such as the cell membrane, integrin's transmembrane domain, and in-
424 tegrin clustering and diffusion^{28,35,63–65} were omitted from our model for simplicity, but could
425 be added as new multiscale mechanobiological questions are posed regarding their mechanics.

Multiscale Integrin Mechanosensing and Cell Adhesion

426 Lastly, our multiscale framework could be broadened to reveal the nano- and micro- mechanics
427 within nascent engineered tissues and organ-chips that apply controllable biophysical loads at the
428 cell membrane^{66–71}.

429 SUPPLEMENTARY MATERIAL

430 See the supplementary material for detailed equations and parameters for the whole-cell model;
431 parameters for the minimization, equilibration, and force distribution analysis of the MD model;
432 RMSD, pressure, and temperature during equilibration; whole-cell model mesh and timestep con-
433 vergence studies; and trajectory movies for the whole-cell and MD models. The whole-cell model
434 is available at <https://github.com/dredremontes/wholeCellFE> and the MD model is avail-
435 able at https://github.com/dredremontes/pull_integrinMD.

436 AUTHOR CONTRIBUTIONS

437 **A.R. Montes:** Conceptualization, data curation, formal analysis, funding acquisition, inves-
438 tigation, methodology, project administration, software, validation, visualization, and writing -
439 original. **G. Gutierrez:** Formal analysis, investigation. **A.B. Tepole:** Conceptualization, data
440 curation, formal analysis, funding acquisition, investigation, methodology, project administration,
441 resources, software, supervision, validation, visualization, writing - original, and writing - review
442 & editing. **M.R.K. Mofrad:** Conceptualization, funding acquisition, project administration, re-
443 sources, supervision, and writing - review & editing.

444 ACKNOWLEDGMENTS

445 This research used Stampede2 at Texas Advanced Computing Center through allocation
446 MCB100146 from Advanced Cyberinfrastructure Coordination Ecosystem: Services & Sup-
447 port (ACCESS) super-computing facilities, supported by the National Science Foundation grants
448 #2138259, #2138286, #2138307, #2137603, and #2138296. A.R.M. was funded by the Ford Foun-
449 dation's Predoctoral Fellowship awarded by the National Academies of Science, Engineering, and
450 Medicine and the Robert N. Noyce Fellowship from UC Berkeley's College of Engineering. G.G.
451 was supported by the National Science Foundation California Alliance for Minority Participation.
452 Thank you to Ghafar Yerima and Nya Domkam for helping set up GROMACS and gromacs-fda.

Multiscale Integrin Mechanosensing and Cell Adhesion

453 We also thank the Molecular Cell Biomechanics Lab and the Berkeley Biomechanics Lab for
454 fruitful discussions that improved the manuscript.

455 DATA AVAILABILITY STATEMENT

456 The data that support the findings of this study are available from the corresponding author
457 upon reasonable request.

458 CONFLICTS OF INTEREST

459 There are no conflicts to disclose.

460 REFERENCES

461 ¹D. E. Ingber, “Mechanosensation through integrins: cells act locally but think globally,” Proceedings of the National Academy of Sciences **100**, 1472–1474 (2003).

462 ²Z. Jahed, H. Shams, M. Mehrbod, and M. R. Mofrad, “Mechanotransduction pathways linking
463 the extracellular matrix to the nucleus,” International review of cell and molecular biology **310**,
464 171–220 (2014).

465 ³J. Zhu, C. V. Carman, M. Kim, M. Shimaoka, T. A. Springer, and B.-H. Luo, “Requirement of
466 α and β subunit transmembrane helix separation for integrin outside-in signaling,” Blood, The
467 Journal of the American Society of Hematology **110**, 2475–2483 (2007).

468 ⁴P. E. Hughes, F. Diaz-Gonzalez, L. Leong, C. Wu, J. A. McDonald, S. J. Shattil, and M. H. Gins-
469 berg, “Breaking the integrin hinge: A defined structural constraint regulates integrin signaling,”
470 Journal of Biological Chemistry **271**, 6571–6574 (1996).

471 ⁵E. Puklin-Faucher and M. P. Sheetz, “The mechanical integrin cycle,” Journal of cell science
472 **122**, 179–186 (2009).

473 ⁶J. Takagi, B. M. Petre, T. Walz, and T. A. Springer, “Global conformational rearrangements in
474 integrin extracellular domains in outside-in and inside-out signaling,” Cell **110**, 599–611 (2002).

475 ⁷S. W. Moore, P. Roca-Cusachs, and M. P. Sheetz, “Stretchy proteins on stretchy substrates:
476 the important elements of integrin-mediated rigidity sensing,” Developmental cell **19**, 194–206
477 (2010).

Multiscale Integrin Mechanosensing and Cell Adhesion

- 479 ⁸J. Deng, C. Zhao, J. P. Spatz, and Q. Wei, “Nanopatterned adhesive, stretchable hydrogel to
480 control ligand spacing and regulate cell spreading and migration,” *ACS nano* **11**, 8282–8291
481 (2017).
- 482 ⁹J. Lee, A. A. Abdeen, D. Zhang, and K. A. Kilian, “Directing stem cell fate on hydrogel sub-
483 strates by controlling cell geometry, matrix mechanics and adhesion ligand composition,” *Bio-*
484 *materials* **34**, 8140–8148 (2013).
- 485 ¹⁰P. Moreno-Layseca, J. Icha, H. Hamidi, and J. Ivaska, “Integrin trafficking in cells and tissues,”
486 *Nature cell biology* **21**, 122–132 (2019).
- 487 ¹¹J. Takagi, K. Strokovich, T. A. Springer, and T. Walz, “Structure of integrin $\alpha 5\beta 1$ in complex
488 with fibronectin,” *The EMBO journal* **22**, 4607–4615 (2003).
- 489 ¹²S. Schumacher, D. Dedden, R. V. Nunez, K. Matoba, J. Takagi, C. Biertümpfel, and N. Mizuno,
490 “Structural insights into integrin $\alpha 5\beta 1$ opening by fibronectin ligand,” *Science Advances* **7**,
491 eabe9716 (2021).
- 492 ¹³T. Nagai, N. Yamakawa, S.-i. Aota, S. S. Yamada, S. K. Akiyama, K. Olden, and K. M. Yamada,
493 “Monoclonal antibody characterization of two distant sites required for function of the central
494 cell-binding domain of fibronectin in cell adhesion, cell migration, and matrix assembly.” *The*
495 *Journal of cell biology* **114**, 1295–1305 (1991).
- 496 ¹⁴I. Wierzbicka-Patynowski and J. E. Schwarzbauer, “The ins and outs of fibronectin matrix as-
497 sembly,” *Journal of cell science* **116**, 3269–3276 (2003).
- 498 ¹⁵J. C. Friedland, M. H. Lee, and D. Boettiger, “Mechanically activated integrin switch controls
499 $\alpha 5\beta 1$ function,” *Science* **323**, 642–644 (2009).
- 500 ¹⁶D. Barkan, L. H. El Touny, A. M. Michalowski, J. A. Smith, I. Chu, A. S. Davis, J. D. Webster,
501 S. Hoover, R. M. Simpson, J. Gauldie, *et al.*, “Metastatic growth from dormant cells induced by
502 a col-*i*-enriched fibrotic environment metastatic outgrowth from dormant tumor cells,” *Cancer*
503 *research* **70**, 5706–5716 (2010).
- 504 ¹⁷J. Z. Kechagia, J. Ivaska, and P. Roca-Cusachs, “Integrins as biomechanical sensors of the
505 microenvironment,” *Nature Reviews Molecular Cell Biology* **20**, 457–473 (2019).
- 506 ¹⁸M. J. Paszek, N. Zahir, K. R. Johnson, J. N. Lakins, G. I. Rozenberg, A. Gefen, C. A. Reinhart-
507 King, S. S. Margulies, M. Dembo, D. Boettiger, *et al.*, “Tensional homeostasis and the malignant
508 phenotype,” *Cancer cell* **8**, 241–254 (2005).
- 509 ¹⁹J. J. Northey, L. Przybyla, and V. M. Weaver, “Tissue force programs cell fate and tumor aggres-
510 sion mechanotransduction in cell fate and cancer aggression,” *Cancer discovery* **7**, 1224–1237

Multiscale Integrin Mechanosensing and Cell Adhesion

- 511 (2017).
- 512 ²⁰F. Li, S. D. Redick, H. P. Erickson, and V. T. Moy, “Force measurements of the $\alpha 5\beta 1$ integrin–
513 fibronectin interaction,” *Biophysical journal* **84**, 1252–1262 (2003).
- 514 ²¹A. C. Chang, A. H. Mekhdjian, M. Morimatsu, A. K. Denisin, B. L. Pruitt, and A. R. Dunn,
515 “Single molecule force measurements in living cells reveal a minimally tensioned integrin state,”
516 *ACS nano* **10**, 10745–10752 (2016).
- 517 ²²M. Benito-Jardon, S. Klapproth, I. Gimeno-LLuch, T. Petzold, M. Bharadwaj, D. J. Müller,
518 G. Zuchtriegel, C. A. Reichel, and M. Costell, “The fibronectin synergy site re-enforces cell
519 adhesion and mediates a crosstalk between integrin classes,” *Elife* **6**, e22264 (2017).
- 520 ²³L. Schrödinger, “The PyMOL molecular graphics system, version 1.8,” (2015).
- 521 ²⁴M. J. Abraham, T. Murtola, R. Schulz, S. Páll, J. C. Smith, B. Hess, and E. Lindahl, “Gro-
522 macs: High performance molecular simulations through multi-level parallelism from laptops to
523 supercomputers,” *SoftwareX* **1**, 19–25 (2015).
- 524 ²⁵W. Humphrey, A. Dalke, and K. Schulten, “VMD – Visual Molecular Dynamics,” *Journal of*
525 *Molecular Graphics* **14**, 33–38 (1996).
- 526 ²⁶L. Treloar, “The elasticity and related properties of rubbers,” *Reports on progress in physics* **36**,
527 755 (1973).
- 528 ²⁷Y. Guo, S. Calve, and A. B. Tepole, “Multiscale mechanobiology: Coupling models of adhesion
529 kinetics and nonlinear tissue mechanics,” *Biophysical Journal* **121**, 525–539 (2022).
- 530 ²⁸B. Cheng, W. Wan, G. Huang, Y. Li, G. M. Genin, M. R. Mofrad, T. J. Lu, F. Xu, and M. Lin,
531 “Nanoscale integrin cluster dynamics controls cellular mechanosensing via faky397 phosphory-
532 lation,” *Science advances* **6**, eaax1909 (2020).
- 533 ²⁹T. Brochu and R. Bridson, “Robust topological operations for dynamic explicit surfaces,” *SIAM*
534 *Journal on Scientific Computing* **31**, 2472–2493 (2009).
- 535 ³⁰W. Chen, J. Lou, J. Hsin, K. Schulten, S. C. Harvey, and C. Zhu, “Molecular dynamics simula-
536 tions of forced unbending of integrin $\alpha v\beta 3$,” *PLoS computational biology* **7**, e1001086 (2011).
- 537 ³¹M. Kulke and W. Langel, “Molecular dynamics simulations to the bidirectional adhesion signal-
538 ing pathway of integrin $\alpha v\beta 3$,” *Proteins: Structure, Function, and Bioinformatics* **88**, 679–688
539 (2020).
- 540 ³²F. Kong, A. J. García, A. P. Mould, M. J. Humphries, and C. Zhu, “Demonstration of catch
541 bonds between an integrin and its ligand,” *Journal of Cell Biology* **185**, 1275–1284 (2009).

Multiscale Integrin Mechanosensing and Cell Adhesion

- 542 33 M. Gao, D. Craig, V. Vogel, and K. Schulten, “Identifying unfolding intermediates of fn-iii10
543 by steered molecular dynamics,” *Journal of molecular biology* **323**, 939–950 (2002).
- 544 34 A. R. Bausch, F. Ziemann, A. A. Boulbitch, K. Jacobson, and E. Sackmann, “Local measure-
545 ments of viscoelastic parameters of adherent cell surfaces by magnetic bead microrheometry,”
546 *Biophysical journal* **75**, 2038–2049 (1998).
- 547 35 T. C. Bidone, A. V. Skeeters, P. W. Oakes, and G. A. Voth, “Multiscale model of integrin
548 adhesion assembly,” *PLOS Computational Biology* **15**, e1007077 (2019).
- 549 36 A. Trache, J. P. Trzeciakowski, L. Gardiner, Z. Sun, M. Muthuchamy, M. Guo, S. Y. Yuan, and
550 G. A. Meininger, “Histamine effects on endothelial cell fibronectin interaction studied by atomic
551 force microscopy,” *Biophysical journal* **89**, 2888–2898 (2005).
- 552 37 X. Wu, Z. Sun, A. Foskett, J. P. Trzeciakowski, G. A. Meininger, and M. Muthuchamy, “Car-
553 diomyocyte contractile status is associated with differences in fibronectin and integrin interac-
554 tions,” *American Journal of Physiology-Heart and Circulatory Physiology* **298**, H2071–H2081
555 (2010).
- 556 38 P. Roca-Cusachs, T. Iskratsch, and M. P. Sheetz, “Finding the weakest link—exploring integrin-
557 mediated mechanical molecular pathways,” *Journal of cell science* **125**, 3025–3038 (2012).
- 558 39 A. F. Oberhauser, C. Badilla-Fernandez, M. Carrion-Vazquez, and J. M. Fernandez, “The me-
559 chanical hierarchies of fibronectin observed with single-molecule afm,” *Journal of molecular
560 biology* **319**, 433–447 (2002).
- 561 40 X. Wang and T. Ha, “Defining single molecular forces required to activate integrin and notch
562 signaling,” *Science* **340**, 991–994 (2013).
- 563 41 M. H. Jo, J. Li, V. Jaumouillé, Y. Hao, J. Coppola, J. Yan, C. M. Waterman, T. A. Springer, and
564 T. Ha, “Single-molecule characterization of subtype-specific $\beta 1$ integrin mechanics,” *Nature
565 communications* **13**, 7471 (2022).
- 566 42 J. L. Young, X. Hua, H. Somsel, F. Reichart, H. Kessler, and J. P. Spatz, “Integrin subtypes
567 and nanoscale ligand presentation influence drug sensitivity in cancer cells,” *Nano Letters* **20**,
568 1183–1191 (2020).
- 569 43 P. Kanchanawong and D. A. Calderwood, “Organization, dynamics and mechanoregulation of
570 integrin-mediated cell–ecm adhesions,” *Nature Reviews Molecular Cell Biology* **24**, 142–161
571 (2023).
- 572 44 J. Li, J. Yan, and T. A. Springer, “Low-affinity integrin states have faster ligand-binding kinetics
573 than the high-affinity state,” *Elife* **10**, e73359 (2021).

Multiscale Integrin Mechanosensing and Cell Adhesion

- 574 ⁴⁵Y. Takada, X. Ye, and S. Simon, “The integrins,” *Genome biology* **8**, 1–9 (2007).
- 575 ⁴⁶N. Strohmeyer, M. Bharadwaj, M. Costell, R. Fässler, and D. J. Müller, “Fibronectin-bound
576 $\alpha 5\beta 1$ integrins sense load and signal to reinforce adhesion in less than a second,” *Nature Materials* **16**, 1262–1270 (2017).
- 578 ⁴⁷Y. Chen, H. Lee, H. Tong, M. Schwartz, and C. Zhu, “Force regulated conformational change
579 of integrin $\alpha v\beta 3$,” *Matrix biology* **60**, 70–85 (2017).
- 580 ⁴⁸N. Li, S. Qiu, Y. Fang, J. Wu, and Q. Li, “Comparison of linear vs. cyclic rgd pentapeptide
581 interactions with integrin $\alpha v\beta 3$ by molecular dynamics simulations,” *Biology* **10**, 688 (2021).
- 582 ⁴⁹A. Malandrino, X. Trepat, R. D. Kamm, and M. Mak, “Dynamic filopodial forces induce ac-
583 cumulation, damage, and plastic remodeling of 3d extracellular matrices,” *PLoS computational
584 biology* **15**, e1006684 (2019).
- 585 ⁵⁰O. Chaudhuri, J. Cooper-White, P. A. Janmey, D. J. Mooney, and V. B. Shenoy, “Effects of
586 extracellular matrix viscoelasticity on cellular behaviour,” *Nature* **584**, 535–546 (2020).
- 587 ⁵¹S. Münster, L. M. Jawerth, B. A. Leslie, J. I. Weitz, B. Fabry, and D. A. Weitz, “Strain history
588 dependence of the nonlinear stress response of fibrin and collagen networks,” *Proceedings of the
589 National Academy of Sciences* **110**, 12197–12202 (2013).
- 590 ⁵²C. Liu, R. Y. Nguyen, G. A. Pizzurro, X. Zhang, X. Gong, A. R. Martinez, and M. Mak,
591 “Self-assembly of mesoscale collagen architectures and applications in 3d cell migration,” *Acta
592 Biomaterialia* **155**, 167–181 (2023).
- 593 ⁵³A. Elosegui-Artola, “The extracellular matrix viscoelasticity as a regulator of cell and tissue
594 dynamics,” *Current Opinion in Cell Biology* **72**, 10–18 (2021).
- 595 ⁵⁴P. Sacco, F. Piazza, C. Pizzolitto, G. Baj, F. Brun, E. Marsich, and I. Donati, “Regulation of
596 substrate dissipation via tunable linear elasticity controls cell activity,” *Advanced Functional
597 Materials* **32**, 2200309 (2022).
- 598 ⁵⁵Y. Ma, T. Han, Q. Yang, J. Wang, B. Feng, Y. Jia, Z. Wei, and F. Xu, “Viscoelastic cell mi-
599 croenvironment: hydrogel-based strategy for recapitulating dynamic ecm mechanics,” *Advanced
600 Functional Materials* **31**, 2100848 (2021).
- 601 ⁵⁶W. Li, D. Wu, D. Hu, S. Zhu, C. Pan, Y. Jiao, L. Li, B. Luo, C. Zhou, and L. Lu, “Stress-relaxing
602 double-network hydrogel for chondrogenic differentiation of stem cells,” *Materials Science and
603 Engineering: C* **107**, 110333 (2020).
- 604 ⁵⁷R. Y. Nguyen, A. T. Cabral, A. Rossello-Martinez, A. Zulli, X. Gong, Q. Zhang, J. Yan, and
605 M. Mak, “Tunable mesoscopic collagen island architectures modulate stem cell behavior,” *Ad-*

Multiscale Integrin Mechanosensing and Cell Adhesion

- 606 vanced Materials **35**, 2207882 (2023).
- 607 ⁵⁸N. J. Hoff, “Approximate analysis of structures in the presence of moderately large creep defor-
608 mations,” Quarterly of Applied Mathematics **12**, 49–55 (1954).
- 609 ⁵⁹Z. Gong, S. E. Szczesny, S. R. Caliari, E. E. Charrier, O. Chaudhuri, X. Cao, Y. Lin, R. L. Mauck,
610 P. A. Janmey, J. A. Burdick, *et al.*, “Matching material and cellular timescales maximizes cell
611 spreading on viscoelastic substrates,” Proceedings of the National Academy of Sciences **115**,
612 E2686–E2695 (2018).
- 613 ⁶⁰N. Wang, J. D. Tytell, and D. E. Ingber, “Mechanotransduction at a distance: mechanically
614 coupling the extracellular matrix with the nucleus,” Nature reviews Molecular cell biology **10**,
615 75–82 (2009).
- 616 ⁶¹S. Wang, E. Stoops, U. Cp, B. Markus, A. Reuveny, E. Ordan, and T. Volk, “Mechanotransduc-
617 tion via the linc complex regulates dna replication in myonuclei,” Journal of Cell Biology **217**,
618 2005–2018 (2018).
- 619 ⁶²S. Tsukamoto, T. Asakawa, S. Kimura, N. Takesue, M. R. Mofrad, and N. Sakamoto, “In-
620 tranuclear strain in living cells subjected to substrate stretching: A combined experimental and
621 computational study,” Journal of Biomechanics **119**, 110292 (2021).
- 622 ⁶³M. J. Paszek, D. Boettiger, V. M. Weaver, and D. A. Hammer, “Integrin clustering is driven by
623 mechanical resistance from the glycocalyx and the substrate,” PLoS computational biology **5**,
624 e1000604 (2009).
- 625 ⁶⁴M. Mehrbod and M. R. Mofrad, “Localized lipid packing of transmembrane domains impedes
626 integrin clustering,” PLoS computational biology **9**, e1002948 (2013).
- 627 ⁶⁵M. Mehrbod, S. Trisno, and M. R. Mofrad, “On the activation of integrin α ii β 3: outside-in
628 and inside-out pathways,” Biophysical journal **105**, 1304–1315 (2013).
- 629 ⁶⁶A. Elosegui-Artola, A. Gupta, A. J. Najibi, B. R. Seo, R. Garry, C. M. Tringides, I. de Lázaro,
630 M. Darnell, W. Gu, Q. Zhou, *et al.*, “Matrix viscoelasticity controls spatiotemporal tissue orga-
631 nization,” Nature Materials , 1–11 (2022).
- 632 ⁶⁷G. R. López-Marcial, A. Y. Zeng, C. Osuna, J. Dennis, J. M. García, and G. D. O’Connell,
633 “Agarose-based hydrogels as suitable bioprinting materials for tissue engineering,” ACS Bio-
634 materials Science & Engineering **4**, 3610–3616 (2018).
- 635 ⁶⁸J. P. McKinley, A. R. Montes, M. N. Wang, A. R. Kamath, G. Jimenez, J. Lim, S. A. Marathe,
636 M. R. Mofrad, and G. D. O’Connell, “Design of a flexing organ-chip to model in situ loading
637 of the intervertebral disc,” Biomicrofluidics **16**, 054111 (2022).

Multiscale Integrin Mechanosensing and Cell Adhesion

- 638 69 J. E. Barthold, B. M. St. Martin, S. L. Sridhar, F. Vernerey, S. E. Schneider, A. Wacquez, V. L.
639 Ferguson, S. Calve, and C. P. Neu, “Recellularization and integration of dense extracellular ma-
640 trix by percolation of tissue microparticles,” Advanced functional materials **31**, 2103355 (2021).
641 70 P. Dhavalikar, A. Robinson, Z. Lan, D. Jenkins, M. Chwatko, K. Salhadar, A. Jose, R. Kar,
642 E. Shoga, A. Kannapiran, *et al.*, “Review of integrin-targeting biomaterials in tissue engineer-
643 ing,” Advanced healthcare materials **9**, 2000795 (2020).
644 71 A. Sontheimer-Phelps, B. A. Hassell, and D. E. Ingber, “Modelling cancer in microfluidic hu-
645 man organs-on-chips,” Nature Reviews Cancer **19**, 65–81 (2019).